Mon. Not. R. Astron. Soc. **000**, 000–000 (0000) Printed 16 March 2015 (MN LATEX style file v2.2)

The impact of mechanical AGN feedback on the formation of massive early-type galaxies

Ena Choi[1,2⋆], Jeremiah P. Ostriker[2,3], Thorsten Naab[4], Ludwig Oser[3], Benjamin P. Moster[5]

[1] *Department of Physics and Astronomy, Rutgers, The State University of New Jersey, Piscataway, NJ 08854, USA*
[2] *Department of Astrophysical Sciences, Princeton University, Princeton, NJ 08544, USA*
[3] *Department of Astronomy, Columbia University, New York, NY 10027, USA*
[4] *Max-Planck-Institut für Astrophysik, Karl-Schwarzschild-Strasse 1, 85741 Garching, Germany*
[5] *Kavli Institute for Cosmology and Institute of Astronomy, Madingley Rd, Cambridge CB3 0HA, UK*

arXiv:1403.1257v2 [astro-ph.CO] 13 Mar 2015

Accepted ???. Received ??? in original form ???

ABSTRACT

We employ cosmological hydrodynamical simulations to investigate the effects of AGN feedback on the formation of massive galaxies with present-day stellar masses of $M_{\rm stel} = 8.8 \times 10^{10} - 6.0 \times 10^{11}\,{\rm M}_{\odot}$. Using smoothed particle hydrodynamics simulations with a pressure-entropy formulation that allows an improved treatment of contact discontinuities and fluid mixing, we run three sets of simulations of 20 halos with different AGN feedback models: (1) no feedback, (2) thermal feedback, and (3) mechanical and radiation feedback. We assume that seed black holes are present at early cosmic epochs at the centre of emerging dark matter halos and trace their mass growth via gas accretion and mergers with other black holes. Both feedback models successfully recover the observed $M_{\rm BH} - \sigma$ relation and black hole-to-stellar mass ratio for simulated central early-type galaxies. The baryonic conversion efficiencies are reduced by a factor of two compared to models without any AGN feedback at all halo masses. However, massive galaxies simulated with thermal AGN feedback show a factor of $\sim 10 - 100$ higher X-ray luminosities than observed. The mechanical/radiation feedback model reproduces the observed correlation between X-ray luminosities and velocity dispersion, e.g. for galaxies with $\sigma = 200$ km s^{-1}, the X-ray luminosity is reduced from 10^{42} erg s^{-1} to 10^{40} erg s^{-1}. It also efficiently suppresses late time star formation, reducing the specific star formation rate from $10^{-10.5}$ yr^{-1} to 10^{-14} yr^{-1} on average and resulting in quiescent galaxies since z=2, whereas the thermal feedback model shows higher late time in-situ star formation rates than observed.

Key words: galaxies: elliptical – quasars: general – quasars: supermassive black holes – galaxies: evolution – methods: numerical

1 INTRODUCTION

There is solid observational evidence that most massive galaxies harbor massive black holes in their centres (Kormendy & Richstone 1995), the masses of which are correlated with the properties of their host galaxies, including bulge mass (Magorrian et al. 1998; Marconi & Hunt 2003), velocity dispersion (Gebhardt et al. 2000; Ferrarese & Merritt 2000; Tremaine et al. 2002), globular cluster systems (Burkert & Tremaine 2010), and many others (see Kormendy & Ho 2013, and references therein). It was proposed that the energy released by the accretion mechanism onto black holes is sufficient enough to unbind galactic interstellar medium and trigger strong outflows (Silk & Rees 1998). This AGN feedback mechanism is confirmed by many observations including the broad absorption lines in the spectra of quasars, the detection of X-ray cavities and radio jets (see Fabian 2012, and references therein).

Without the inclusion of AGN feedback traditional numerical cosmological simulations of the formation of massive early-type galaxies suffer from the 'overcooling' problem: over a Hubble time too much cold gas is able to cool at the centres of the galaxy halos (Katz & White 1993). This leads to overly massive and actively star-forming ellipticals at present, in contradiction with observations (e.g. Kauffmann et al. 2003; Franx et al. 2008) and basic predictions of ΛCDM structure formation (e.g. Moster et al. 2010).

⋆ E-mail:enachoi@physics.rutgers.edu

Many semi-analytical models of galaxy formation, extended by various models for AGN feedback, have demonstrated that this process is relevant for reproducing the bright end of the galaxy luminosity function (Bower et al. 2006; Croton et al. 2006; De Lucia & Blaizot 2007; Somerville et al. 2008; Guo et al. 2011). Dynamically and spatially better resolved direct hydrodynamical cosmological simulations including AGN feedback confirm that this mechanism is able to self-regulate the stellar baryon content in massive halos resulting in more realistic galaxy masses and colours, and that it can reproduce the relations between black hole mass and bulge mass ($M_{\rm BH} - M_{\rm b}$) and stellar velocity dispersion $M_{\rm BH} - \sigma$ (e.g. Sijacki et al. 2007; Booth & Schaye 2011; Teyssier et al. 2011; Martizzi et al. 2012; Vogelsberger et al. 2013).

Many previous AGN feedback models include only a subset of the known and observed feedback processes. Since the importance of AGN-driven mass and momentum outflows in limiting the infall onto the black hole has been emphasized (see Murray et al. 2005; Ostriker et al. 2010; Debuhr et al. 2010, 2011), in previous works (Choi et al. 2012, 2014) we proposed a mechanical and radiative AGN feedback together with the detailed treatment of radiative heating, radiation pressure, and the Eddington force from black holes and investigated the effects of the new AGN feedback model. It is shown that the new feedback model can regulate the black hole growth, and successfully reproduce the observed and $M_{\rm BH} - \sigma$ relation in a way similar to the successful thermal feedback approach (Springel et al. 2005). But as pointed out in McCarthy et al. (2010), the X-ray output is sensitive to AGN feedback. The commonly adopted thermal feedback model where all the feedback energy is distributed as local thermal heating produces a factor of $\sim$100 higher thermal X-ray luminosity than expected for a given stellar mass of the galaxy while the new approach reproduces the observed $L_X - \sigma$ (Choi et al. 2012, 2014). The physical reason for this is simple: momentum input from AGN winds and radiation efficiently drives gas out into the surrounding halo, reducing the central density and thermal X-ray luminosity. The two treatments - thermal vs mechanical - put in the same total energy for a given accretion rate and given efficiency, but putting some fraction of the energy into mechanical rather than thermal increases the effectiveness in driving gas out of the galaxy. The same result was found in supernova feedback (Simpson et al. 2014). The mechanical feedback model also shows large fluctuations in both radiant and wind outputs, in agreement with observations (see also Debuhr et al. 2012).

In a next step we now aim at characterizing the evolution of galaxies and black holes with mechanical and radiation AGN feedback in a full cosmological context. Even though numerical limitations impose inevitable approximations in the form of sub-resolution models, cosmological simulations can provide a more complete view on the evolution of galaxies and their central black holes, starting from initial conditions consistent with the early universe as specified by the WMAP (Spergel et al. 2003) and Planck satellites (Planck Collaboration et al. 2013). In order to statistically confront observations, we need a cosmological sample of massive galaxies and black holes that covers a wide range of environments and redshifts.

In this paper, we investigate the effects of mechanical and radiation AGN feedback on the cosmological formation of individual galaxies with three sets of cosmological, hydrodynamical zoom simulations of 20 halos in the mass range $2.3 \times 10^{12}\,{\rm M}_\odot \lesssim M_{\rm vir} \lesssim 1.4 \times 10^{13}\,{\rm M}_\odot$. This extends the recent studies by Oser et al. (2010, 2012), on which our initial conditions are based, but did not contain AGN feedback. In the three simulation sets, we add the commonly adopted thermal AGN feedback and our mechanical and radiation AGN feedback separately to investigate their impact on black hole growth, the conversion of gas into stars, star formation, and thermal X-ray luminosity of hot gas.

The paper is organized as follows. Section 2 provides an introduction to our simulations and the adopted AGN feedback model. In section 3, we discuss the effect of AGN feedback on black hole growth, black hole and galaxy scaling relations, X-ray luminosities of hot gas, baryonic stellar and gas mass fraction, star formation rates, galaxy sizes and velocity dispersions. A final summary and discussion of this work is given in section 4.

2 SIMULATIONS

2.1 Numerical code

The simulations presented in this paper were performed with a modified version of the parallel smoothed particle hydrodynamics (SPH) code GADGET-3 (Springel 2005). Although SPH has many advantages, such as the exact conservation of physical properties and the adaptive resolution, recent studies have shown that standard SPH has severe difficulties in modeling fluid mixing owing to spurious surface tension at contact discontinuities (e.g. Agertz et al. 2007). To avoid the numerical artifacts we have used SPHGAL a modified version of GADGET with improved accuracy. Details of the code are presented in Hu et al. (2014), in the following we give a brief overview.

The code includes a density-independent SPH formulation by choosing a different volume element (Ritchie & Thomas 2001; Saitoh & Makino 2013). Specifically, we employ the pressure-entropy formulation as described in Hopkins (2013). Furthermore, we improve the force accuracy of our method by increasing the particle number in the kernel. To avoid the pairing instability we adopt the Wendland C^4 kernel with 200 neighboring particles (Dehnen & Aly 2012). To further improve over standard SPH we use the improved artificial viscosity implementation presented by Cullen & Dehnen (2010). In this scheme each SPH particle has a variable viscosity coefficient which only increases when a converging flow is detected and afterwards decays to a minimum in a few sound-crossing times such that unwanted viscosity away from shocks is suppressed. To detect shocks in advance, the time derivative of the velocity divergence is used. We further include an artificial thermal conductivity following Read & Hayfield (2012) which smoothes the internal energy while explicitly conserving it within the kernel. While this seems to be redundant in the pressure-entropy formulation, in strong shocks the entropy jumps can be very high resulting in very noisy pressure estimates. Artificial diffusion is reduced away from entropy discontinuities with a switch similar to the one used for artificial viscosity. Finally we employ a time-step limiter following Saitoh

Table 1. Full list of parameters of the two AGN models

parameters	ThAGN[a]	MrAGN
$M_{\rm BHseed}$	$10^5\,h^{-1}\,{\rm M}_\odot$	$10^6\,h^{-1}\,{\rm M}_\odot$
$M_{\rm halo}$	$5\times10^{10}\,h^{-1}\,{\rm M}_\odot$	$10^{11}\,h^{-1}\,{\rm M}_\odot$
α	100	1
$\epsilon_{\rm f}$	0.005	0.002

[a] Note that we use the standard mass accretion prescription and parameters used in the previous works (e.g. Sijacki et al. 2007), which produce a broad agreement with observational constraints.

& Makino (2009); Durier & Dalla Vecchia (2012) to ensure that neighboring particles have similar time-step (within a factor of 4), such that ambient particles do not remain inactive when a shock is approaching. The performance of the new SPH schemes in the test problems is discussed in Hu et al. (2014).

For the star formation and feedback prescription we use the self-regulated supernova feedback model of Springel & Hernquist (2003). This model treats the interstellar medium (ISM) as a two-phase medium (McKee & Ostriker 1977) where clouds of cold gas are embedded in the hot gas phase at pressure equilibrium. Stars are allowed to form out of the cold gas phase if the local density exceeds a threshold value ($n > n_{th} = 0.205\,{\rm cm}^{-3}$) which is calculated self-consistently in a way that the equation of state is continuous at the onset of star formation. Finally the simulations include a cooling prescription for a primordial composition of hydrogen and helium and a redshift-dependent UV background radiation field with a modified Haardt & Madau (1996) spectrum.

2.2 Simulation setup

We use the cosmological 'zoom-in' initial conditions which are described in detail in Oser et al. (2010). The halos are picked from a dark matter only simulation using a flat cosmology with parameters obtained from WMAP3 (Spergel et al. 2007): $h = 0.72$, $\Omega_{\rm b} = 0.044$, $\Omega_{\rm dm} = 0.216$, $\Omega_\Lambda = 0.74$, $\sigma_8 = 0.77$ and an initial slope of the power spectrum of $n_{\rm s} = 0.95$. From redshift zero we trace back in time all particles close to the halos of interest at any given snapshot. Those particles are then replaced with high-resolution gas and dark matter particles. The original dark matter particles are merged to reduce the particle count and the simulation time depending on their distance to the re-simulated halo. The new high resolution zoom-in initial conditions are evolved from redshift z=43 to the present day.

The simulated halo masses cover the range $2.3\times10^{12}\,{\rm M}_\odot \lesssim M_{\rm vir} \lesssim 1.4\times10^{13}\,{\rm M}_\odot$ and the central galaxy masses are between $8.8\times10^{10}\,{\rm M}_\odot \lesssim M_* \lesssim 6.0\times10^{11}\,{\rm M}_\odot$ at $z = 0$. The masses for the gas and star particles are $m_{*,gas} = 4.2\times10^6\,h^{-1}\,{\rm M}_\odot$ (Note that we spawn one star particle per gas particle), whereas the dark matter particles have a mass of $m_{\rm dm} = 2.5\times10^7\,h^{-1}\,{\rm M}_\odot$. The comoving gravitational softening lengths used are $\epsilon_{\rm gas,star} = 400\,{\rm pc\,h^{-1}}$ for the gas and star particles and $\epsilon_{\rm halo} = 890\,{\rm pc\,h^{-1}}$ for the dark matter scaled with the square root of the mass ratio (Dehnen 2001). In the following we present the results for 20 galaxies with masses larger than $M_* \approx 8.8\times10^{10}\,{\rm M}_\odot$ for direct comparison with observations. These galaxies are well resolved with $\approx 1.2-6.8\times10^5$ particles within the virial radius. Using the above simulation parameters for zoom simulations has been shown to result in galaxies with reasonable present-day properties (Naab et al. 2007; Johansson et al. 2009; Naab et al. 2009; Oser et al. 2010). However, Oser et al. (2010) shows that the fraction of available baryons converted into stars, f_*, for galaxies in this mass range is typically 2 times higher than estimates from models that are constructed by matching observed luminosity functions to simulated halo mass functions (Moster et al. 2010; Guo et al. 2010; Behroozi et al. 2010; Moster et al. 2013, and references therein).

In order to study the effects of numerical resolution, we run the high resolution simulation for a high-mass halo with $M_{\rm vir} \sim 5.0\times10^{12}\,{\rm M}_\odot$. The high resolution initial condition has twice better spatial resolution and eight times better mass resolution than our fiducial resolution (i.e. $\epsilon_{\rm gas,star} = 200\,{\rm pc\,h^{-1}}$ and $m_{*,gas} = 5.3\times10^5\,h^{-1}\,{\rm M}_\odot$).

2.3 Black hole formation and growth

In our cosmological simulations of structure formation black holes are modeled as collisionless sink particles which form in newly emerging dark matter halos. We assume that black holes are seeded such that any halo above a certain threshold mass contains one black hole at its centre. We identify haloes on the fly during a simulation by calling a friends-of-friends (FOF) algorithm at regular intervals. All halos with a mass larger than $M_{\rm halo} = 10^{11}\,h^{-1}\,{\rm M}_\odot$ are provided one black hole with mass of $M_{\rm BHseed} = 10^6\,h^{-1}\,{\rm M}_\odot$ if they do not contain any black hole already. The black hole seed mass and halo threshold mass are chosen to roughly follow the Magorrian relation (Magorrian et al. 1998) and the chosen seed mass is small enough that it only makes a negligible contribution to the mass of the final black hole. Growth of supermassive black holes has been previously modeled with full cosmological hydrodynamical simulations with the chosen black hole seed mass ranges from $10^5\,h^{-1}\,{\rm M}_\odot$ to $10^6\,h^{-1}\,{\rm M}_\odot$, and a threshold mass for halo from $10^9\,h^{-1}\,{\rm M}_\odot$ to $10^{11}\,h^{-1}\,{\rm M}_\odot$, and it is shown that these seeds evolve into a population of supermassive black holes with masses and accretion luminosities in line with observational estimates by $z \sim 6$ (Sijacki et al. 2009; Di Matteo et al. 2012; Khandai et al. 2012; DeGraf et al. 2012). It has also been shown that the AGN behavior is not particularly sensitive to the seed mass (Hopkins et al. 2006).

The mass of black holes is assumed to grow via two channels: mergers with other black holes and accretion of gas. Two black hole particles are allowed to merge if they fall within their local SPH smoothing lengths and if their relative velocities are smaller than the local sound speed. The rate of the gas infall onto the black hole is estimated with a Bondi-Hoyle-Lyttleton parameterization (Hoyle & Lyttleton 1939; Bondi & Hoyle 1944; Bondi 1952) with an alternative averaging method introduced in Choi et al. (2012). For gas with the density ρ, a sound speed $c_{\rm s}$ and the velocity relative to the black hole v, the mass accretion rate onto the central region is:

$$\dot{M}_{\rm inf} = \left\langle \frac{4\pi G^2 M_{\rm BH}^2 \rho}{(c_{\rm s}^2+v^2)^{3/2}} \right\rangle, \qquad (1)$$

where angle brackets denote the averaging over the SPH ker-

nel. This method for the calculation of the black hole mass does the calculation in both time and space on an individual particle basis and then averages the results over the neighboring 64 particles in order to reduce the dependency on the number of SPH particles.

To avoid the unphysical accretion of unbound gas from outside the Bondi radius which occurs in some treatments of this problem we statistically limit the accretion of mass to the gas within the Bondi radius. Since the mass distribution of each gas particle is smoothed with the kernel size, we allow for the full accretion rate only if the total volume of a gas particle resides within the Bondi radius. Otherwise, we reduce the probability of being absorbed by the black hole (soft Bondi radius criterion, see Choi et al. (2012)). To account for the time that it takes a particle at radius r_j to be accreted, we include the free-fall modification to the accretion probability with an extra factor of

$$p_{j,\mathrm{ff}} = \frac{\frac{1}{\tau_j}}{\frac{1}{N_{\mathrm{sph}}}\sum_{j=1}^{N_{\mathrm{sph}}}\frac{1}{\tau_j}}, \quad (2)$$

where $\tau_j = r_j/(c_{\mathrm{s},j}^2 + v_j^2)^{1/2}$ is the free fall time and N_{sph} denotes the typical number of smoothing neighboring gas particles of the black hole. For a full description of the soft Bondi radius criterion and the free-fall modification, see Figure 1 and section 2.4 of Choi et al. (2012).

We do not employ an additional factor 'α' with regard to the accretion rate. This has been utilized to overcome resolution problems and better match reality, but adopting it increases the uncertainty of the numerical treatment (Booth & Schaye 2009).

2.4 Mechanical and radiation black hole feedback

Motivated by observations of broad absorption line winds, which convey energy, mass and momentum into the surrounding gas with velocity $\sim 10,000$ km s^{-1} outflows corresponding to a typical broad line wind velocity (Crenshaw et al. 2003; Moe et al. 2009; Dunn et al. 2010), we included these observed AGN winds in our numerical treatment following Ostriker et al. (2010). In our model, the AGN winds carry a mass given by:

$$\dot{M}_{\mathrm{outf}} = \dot{M}_{\mathrm{inf}} - \dot{M}_{\mathrm{acc}}, \quad (3)$$

where $\dot{M}_{\mathrm{outf}}$, $\dot{M}_{\mathrm{inf}}$ and $\dot{M}_{\mathrm{acc}}$ respectively denote the outflowing/inflowing mass rate and the mass rate actually accreted onto the black hole. For simplicity we assume that the wind is launched at a fixed speed $v_{\mathrm{w}} = 10,000$ km s^{-1}. Then a momentum flux carried by the wind is given as,

$$\dot{p} = \dot{M}_{\mathrm{outf}} v_{\mathrm{w}}, \quad (4)$$

and the kinetic energy rate of the outflow is given as,

$$\dot{E}_{\mathrm{w}} \equiv \epsilon_{\mathrm{f}} \dot{M}_{\mathrm{acc}} c^2, \quad (5a)$$

$$= \frac{1}{2}\dot{M}_{\mathrm{outf}} v_{\mathrm{w}}^2, \quad (5b)$$

where ϵ_{f} denotes the feedback efficiency. We can define the dimensionless quantity ψ, the ratio of the mass outflow rate to the accreted rate as,

$$\psi \equiv 2\epsilon_{\mathrm{f}} c^2 / v_{\mathrm{w}}^2 = \dot{M}_{\mathrm{outf}}/\dot{M}_{\mathrm{acc}}, \quad (6)$$

and we can rewrite the equation for the black hole accretion rate as,

$$\dot{M}_{\mathrm{acc}} = \dot{M}_{\mathrm{inf}} \frac{1}{1+\psi}. \quad (7)$$

As discussed in Ostriker et al. (2010); Choi et al. (2012) in the presence of significant AGN winds, not all of the mass entering the central region $\dot{M}_{\mathrm{inf}}$ actually reaches the black hole. For example, with the feedback efficiency typically adopted in the literature, $\epsilon_{\mathrm{f}} = 0.005$, and with the fixed wind velocity $v_{\mathrm{w}} = 10,000$ km s^{-1}, equation (6) and (7) which are based on mass and energy conservation indicate that only 10 percent of the inflowing mass is actually accreted onto the black hole while 90 percent is ejected in a wind.

We calculate the dimensionless quantity ψ for the given feedback efficiency ϵ_{f} and wind velocity v_{w}, and stochastically select the wind particles from all gas particle attracted into the central zone by the black hole keeping the fraction of wind particles to the total inflowing particles as $\psi/(1+\psi)$. To deposit the wind mass and momentum, we give kicks to the gas particles selected following the stochastic approach. We set the direction of the wind to be parallel or anti-parallel to the direction of angular momentum of each gas particle, if the central black holes are surrounded by a gas disc this procedure results in a wind perpendicular to the disc plane (Proga & Kallman 2004). The emitted wind particles share their momentum with two other nearby gas particles to reproduce the shock heated momentum-driven flows. They have the same velocity increment, $\Delta v \sim 10,000/3$ km s^{-1}, conserving the momentum. But sharing momentum with other particles via inelastic collisions decreases the total kinetic energy increment while preserving momentum. We deposit the residual energy into these three particles in thermal form so that the total energy is conserved. Having momentum sharing with two nearby gas particles gives 2:1 divisions into thermal and kinetic energies so the wind particles can reach very high temperatures. This ratio is similar to that in the standard Sedov-Taylor self-similar blast wave.

In addition to the mechanical feedback described above, X-ray radiation from the accreting black hole can be coupled to the surrounding gas according to an approximation described in Sazonov et al. (2005), as in Ciotti et al. (2010); Novak et al. (2011); Choi et al. (2012, 2014); The luminosity flux from the multiple black holes is calculated at the position of each gas particle, and the flux is converted to the net volume heating rate $\dot{E}$ by adopting the Sazonov et al. (2005) formulae that include Compton heating and photoionization heating. Note that Equation 7, not Equation 1, determines the AGN luminosity flux and thus the magnitude of the radiation feedback. We also include the electromagnetic momentum, the radiation pressure from the X-ray flux from the black hole by adding a momentum per unit time of $\dot{p} = \dot{E}/c$. The added force is directed radially away from the black holes.

The flux from UV bump in AGN spectrum dominates for the momentum driven winds as shown in high resolution hydrodynamical simulations (e.g. Proga et al. 2000). The region where this driving occurs is very close to the quasar so we include this in sub-grid modeling, as in "mechanical feedback". And the radiation heating and its associated radiation pressure are from the moderately hard X-ray region (~ 50 keV), which dominates the heating process. Thus

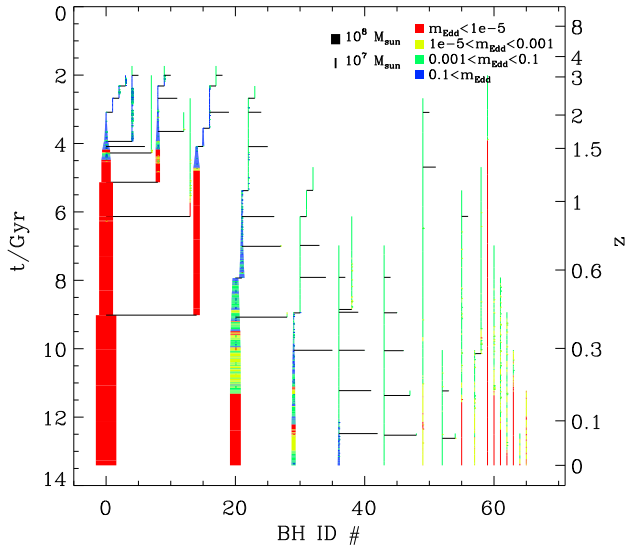

Figure 1. A mass assembly tree of black holes in a sample zoom-in region with mechanical and radiation AGN feedback. Each line represents a black hole and the thickness of the lines is scaled by the mass of the black hole. Mass accretion rate onto the black hole is colour-coded in Eddington units, as black hole mass accretion with Eddington ratio $m_{\rm Edd} < 10^{-5}$ shown in red, $10^{-5} < m_{\rm Edd} < 10^{-3}$ in yellow, $10^{-3} < m_{\rm Edd} < 10^{-1}$ in green, and $10^{-1} < m_{\rm Edd}$ in blue. In total 66 black holes are seeded in this zoom-in region, after black hole mergers 16 black holes survive to $z = 0$. The leftmost branch of the merger tree shows the central black hole with a final mass of $\sim 2.2 \times 10^8\, h^{-1}\, {\rm M}_\odot$ which resides in a main halo with a mass of $\sim 5 \times 10^{12}\, h^{-1}\, {\rm M}_\odot$. The left-right positioning of the progenitors is schematic, and is not connected to the position within the dark matter halo.

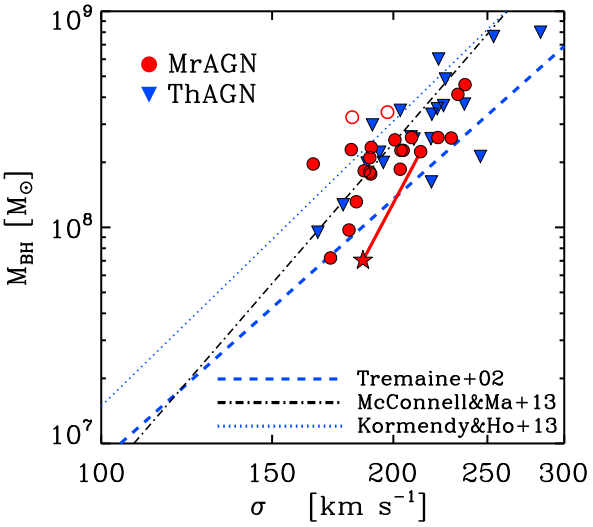

Figure 2. The black hole mass-stellar velocity dispersion ($M_{\rm BH} - \sigma$) relation at $z = 0$ of the two AGN feedback models: thermal feedback (ThAGN, blue upside down triangles) and momentum and radiative feedback (MrAGN, red circles). The red star symbol shows the higher resolution run for one halo MrAGN model and red solid line connects the corresponding lower resolution run. The momentum feedback runs without radiative feedback are shown in open red circles for two halos. The black/blue dotted lines show the observed relation of the early type galaxies from McConnell & Ma (2013) and Kormendy & Ho (2013) respectively.

the momentum in the AGN UV emission is included indirectly by the absorption of the broad absorption line wind that has been accelerated by the metal line trapping (Proga et al. 2000), and the momentum in the X-ray bump is partially allowed for in so far as the X-rays have been absorbed following a standard atomic physics treatment.

Finally, instead of limiting the maximum accretion rate to the Eddington rate, we compute the Eddington force acting on the surrounding gas particles, directed radially away from the black hole as described in Choi et al. (2012) and allow this force to act on the gas flow through the hydrodynamic equations. Naturally it reduces the inflow and increases the outflow but accretion exceeding the Eddington rates can occasionally occur.

In order to study the effects of different AGN feedback models, we investigate the influence on galaxy separately by running the full set of simulations with three different model:

(1) NoAGN: No black hole and no AGN feedback. This model is comparable to the results of Oser et al. (2010, 2012), but note that we use an alternative formulation of SPH designed to treat contact discontinuities more accurately, and include an improved artificial viscosity and an energy diffusion implementation.

(2) ThAGN: with black hole and the classical thermal AGN feedback. Note that we use the standard mass accretion prescription and parameters adopted and studied in the previous works of Sijacki et al. (2007, 2009), i.e. $10^5\, h^{-1}\, {\rm M}_\odot$ for black hole seed mass, $5 \times 10^{10}\, h^{-1}\, {\rm M}_\odot$ for threshold halo mass of the black hole seeding, and $\epsilon_{\rm f} = 0.005$ for AGN feedback efficiency which produce a broad agreement with observational constraints.

(3) MrAGN: with black hole and mechanical and radiation AGN feedback. This model includes the modified black hole mass accretion described in Section 2.3. We use lower feedback efficiency $\epsilon_{\rm f} = 0.002$ for this model which was constrained based on our previous small scale simulations (Choi et al. 2014). The adopted black hole and AGN feedback related parameters are shown in Table 1.

We only consider the central galaxies within the simulated halos and their black holes in this study.

3 COSMOLOGICAL SIMULATIONS OF AGN FEEDBACK IN INDIVIDUAL GALAXY HALOS

3.1 Black hole growth

In order to show how individual black holes grow in our simulations, we show in Figure 1 an example of the mass assembly history of black holes in a sample zoom-in region which forms a main halo with a mass of $\sim 5 \times 10^{12}\, h^{-1}\, {\rm M}_\odot$ at $z = 0$ with the MrAGN model. Each line represents a black hole and the thickness of the lines is scaled by the mass of the black hole. Mass accretion onto the black hole is colour-coded in Eddington units, as black hole mass accretion with Eddington ratio $m_{\rm Edd} < 10^{-5}$ shown in red, $10^{-5} < m_{\rm Edd} < 10^{-3}$ in yellow, $10^{-3} < m_{\rm Edd} < 10^{-1}$ in green, and $10^{-1} < m_{\rm Edd}$ in blue. In total 66 black holes

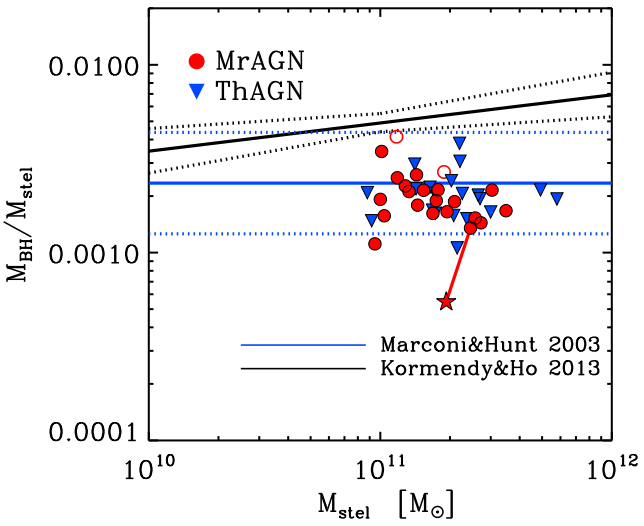

Figure 3. The black hole mass-to-stellar mass ratio at $z = 0$ is plotted against stellar mass for two AGN feedback models: thermal feedback (ThAGN, blue upside down triangles) and momentum and radiative feedback (MrAGN, red circles). The high resolution run with momentum feedback is shown in star symbol with the red solid line that connects the corresponding low resolution run. The momentum feedback runs without radiative feedback are shown in open red circles for two halos. The blue and black solid lines show the observed relation from Marconi & Hunt (2003) and Kormendy & Ho (2013) respectively with an intrinsic dispersion shown in dotted lines.

are seeded, after black hole mergers only 16 black holes survive to $z = 0$. The left–right positioning of the progenitors is schematic, and has no relevance to spatial positions of galaxies within the dark matter halo. The leftmost branch of the merger tree shows the central black hole with a final mass of $\sim 2.3 \times 10^8\,\mathrm{M}_\odot$. At $z = 0$, the most massive black hole is growing less rapidly than less massive black holes. At higher redshift, this trend is greatly diminished, and at z = 2 it is reversed so that the most massive black holes have the highest fractional accretion rate. This phenomenology broadly agrees with the observed 'cosmic downsizing' of AGN, i.e. the most massive and luminous AGN were most numerous at redshift $z \sim 2-2.5$, less luminous AGN peaked at successively lower redshifts with the least luminous peaking at around $z \sim 1$ in X-rays (e.g. Ueda et al. 2003), and in optical and other bands (e.g. Rigby et al. 2011).

We now study how the black hole masses relate to their host galaxies. For this purpose, we determine the central galaxy properties using a spherical over-density criterion at $z = 0$. Following previous studies (e.g. Oser et al. 2012), we obtain a radius where the spherical over-density drops below 200 times the critical density of the universe for a virial radius of the halo, $r_{\rm vir}$, and the virial mass $M_{\rm vir}$ is defined by total mass therein. We then determine the effective radius of the galaxy $r_{\rm eff}$ by getting the mean values of the half-mass radii of all stars within 10% of the virial radius $r_{10} = 0.1 \times r_{\rm vir}$ projected along the three principal axes of the main stellar body. The line-of-sight velocity dispersions σ have been calculated within $0.5 \times r_{\rm eff}$ along the three principal axes and then averaged.

In Figure 2, we show the relation between black hole mass and stellar velocity dispersion σ for the two feedback models. Blue upside down triangles are for the simulations with the classical thermal AGN feedback, ThAGN, while red circles are for the simulations with the mechanical and radiation AGN feedback, MrAGN. Note that two feedback models are tested for the same set of 20 halos. We overplot the observed $M_{\rm BH}-\sigma$ relations as presented in recent papers by McConnell & Ma (2013) (black) and Kormendy & Ho (2013) (blue) respectively. We find a good agreement with the observations for both AGN feedback models as found in our previous study on the bulge dominated merger remnants of the two disc galaxies (Choi et al. 2014). In previous works on black hole growth with the classical thermal AGN feedback (e.g. Sijacki et al. 2007; Di Matteo et al. 2008), a measurement of the $M_{\rm BH} - \sigma$ relation for the simulated galaxies was also found to successfully produce the observed black hole - bulge relations. Note that we use the parameters adopted in Sijacki et al. (2007), but we use the modified version of GADGET-3 code with an alternative formulation of SPH, an updated artificial viscosity and an energy diffusion implementation. The modifications of the code we include in this study do not change their main findings on the black hole mass and bulge relation in general.

In order to study the relative effect of radiation feedback, we perform the control runs for two halos including only the mechanical wind feedback. The results from control run without the radiative feedback are shown in open red circles. The radiative feedback shows moderate impact on the growth of black hole, but the differences are within the observed scatters.

We also perform a resolution study for our primary example with a halo mass of $5 \times 10^{12}\,h^{-1}\,\mathrm{M}_\odot$ with MrAGN feedback. The high resolution run with twice better spatial resolution and with eight times better mass resolution is shown in red star symbol with the red solid line connecting corresponding fiducial resolution run. The resolution has a strong effect both on the velocity dispersion (the final stellar mass) of the galaxy and on the final black hole mass. In higher resolution the final black hole mass is lower by a factor of 3, and this indicates that with resolution increased the black hole feedback becomes slightly more efficient. As the differences induced by increasing resolution are within the observed uncertainties on M-sigma relation, we restrict our main study to our fiducial resolution in this paper. The convergence will be further studied and discussed in later papers.

Figure 3 shows the black hole–to–stellar mass ratio as a function of galaxy stellar mass for the simulated two feedback models: blue upside down triangles are for ThAGN models and red circles are for MrAGN models. The observed relations from Marconi & Hunt (2003) and Kormendy & Ho (2013) are shown in blue lines and black lines respectively. The simulated relations at $z = 0$ for both AGN feedback models match the locally observed canonical black hole–to–bulge mass ratio 0.23% from Marconi & Hunt (2003) well, but the simulated ratios are ~ 2 times lower than the most recent relation found by Kormendy & Ho (2013) who strictly limit their samples and omit all pseudo bulges and merging galaxies. Since we have not made such a restriction for measuring stellar mass in our simulated galaxies, our result would be more appropriately compared to the previously

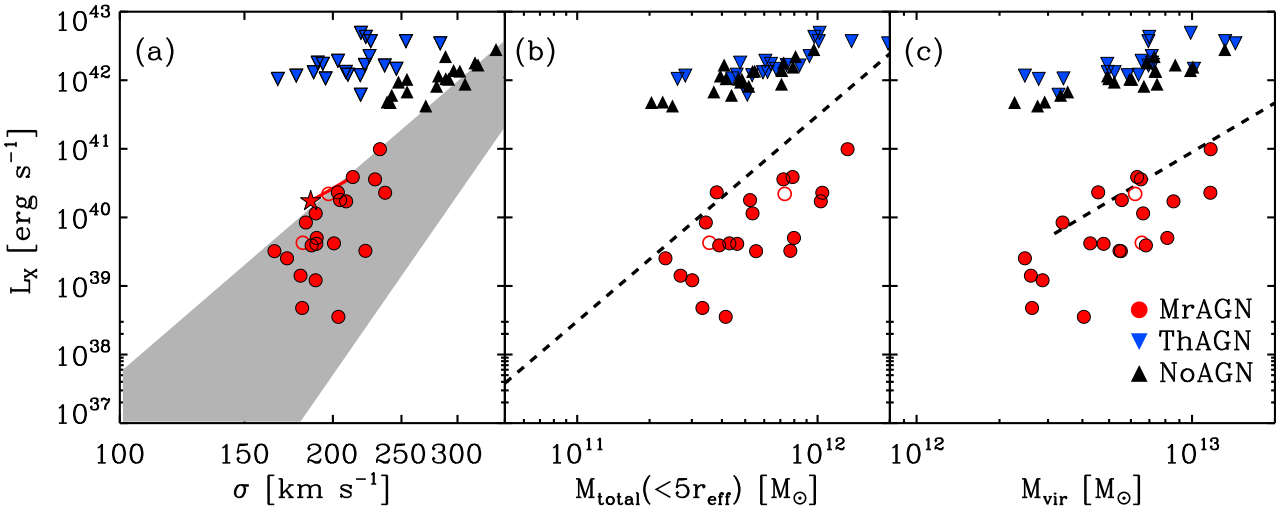

Figure 4. X-ray luminosity versus (a) stellar velocity σ, (b) total mass within $5r_{\rm eff}$, and (c) virial mass $M_{\rm vir}$ of the simulated galaxies at $z = 0$ for the model without AGN feedback (NoAGN, black triangles), thermal feedback (ThAGN, blue upside down triangles), and momentum and radiative feedback (MrAGN, red circles). The high resolution run with momentum feedback is shown in star symbol with the red solid line that connects the corresponding low resolution run. The momentum feedback runs without radiative feedback are shown in open red circles for two halos. Observed relations for the normal early-type galaxies are from (a) Boroson et al. (2011), (b) Kim & Fabbiano (2013), and (c) Mathews et al. (2006) respectively. The simulations without AGN feedback and with thermal AGN feedback show systematically higher X-ray luminosities than observed.

found values of the canonical black hole–to–bulge mass ratios.

3.2 Impact of AGN feedback on X-ray luminosity

The thermal AGN feedback prescription adopted in many previous AGN feedback studies hides the small-scale physics such as radiation-driven winds and shocks under a simple parameterization of local input, and only treats the resulting effects of feedback. As a result, the gas is simply heated near the black hole and produces a very large thermal X-ray luminosity. In the mechanical AGN feedback model, however, the X-ray luminosity is lower, because the outflowing gas carries off significant kinetic energy, which tends to drive gas away from the galaxy, reduce its density and significantly reduce its thermal X-ray output. Hence comparing our simulations with the observations of X-ray scaling relations of nearby early type galaxies (e.g. Forman et al. 1985; Trinchieri & Fabbiano 1985; Mathews & Brighenti 2003; Humphrey et al. 2006) should give us a clean discriminant between the AGN feedback models.

We calculate the X-ray luminosity due to bremsstrahlung radiation as well as line emission from all relevant species in *Chandra* bands (0.3-8 keV) for the simulated central elliptical galaxies using the tools developed in Choi et al. (2014). In order to exclude the star forming gas in the obscured central region of the galaxy, we only include the hot and diffuse gas within the virial radius with a temperature and density cut of $T \geqslant 10^6$ K, and $\rho \leqslant 3.16 \times 10^{-3}\,{\rm M_\odot pc^{-3}}$, which corresponds to the critical density for star formation.

In Figure 4, we show the X-ray luminosity of the hot gas against (a) the stellar velocity dispersion σ, (b) total mass within $5r_{\rm eff}$, and (c) virial mass $M_{\rm vir}$ of the simulated galaxies at $z = 0$ for the simulated central galaxies with three feedback models. Observed relations for the normal early-type galaxies are from (a) Boroson et al. (2011), (b) Kim & Fabbiano (2013), and (c) Mathews et al. (2006) respectively. Observationally all galaxies with a shallow potential well with $\sigma < 200$ km s^{-1} seem to have only a small amount of hot gas with $L_X < 10^{40}$ erg s^{-1} (Boroson et al. 2011), however, ThAGN models show much higher X-ray luminosity for up to $\sim$ 2-3 orders of magnitude higher. On the other hand, MrAGN models produce X-ray luminosity within the observed range, with the two orders of magnitude spread in L_X. Note that we obtain higher X-ray luminosity L_X for ThAGN models compared to the work by Cox et al. (2006), who studied the X-ray luminosity and the scaling relation of merger remnants. This discrepancy seems to be due to the differences in X-ray bandwidths, the inclusion of metal-line emission and the SPH formulation. We use the X-ray luminosity in *Chandra* bands (0.3-8 keV) including bremsstrahlung radiation and metal-line emission from all relevant species, while Cox et al. (2006) used bolometric X-ray luminosity and partially included metal line emission (for 0.1 to 2 KeV). Cox et al. (2006) used the standard formation of SPH which tends to suppress mixing and cooling of the hot gas and result in lower X-ray luminosity.

3.3 Baryonic mass budget

Fig. 5 shows the conversion efficiencies of the simulated galaxies at redshift zero $f_* = m_*/(f_b * m_{vir,dark})$ where m_* is the stellar mass within 10 % of the virial radius r_{10}, $f_b = \Omega_b/\Omega_{dm} = 0.17$ is the cosmic baryon fraction and $m_{vir,dark}$ is the dark matter mass within the virial radius of the galaxy. The amount of total baryonic matter available in each halo is $f_b * m_{vir,dark}$ and then we calculate f_*, the

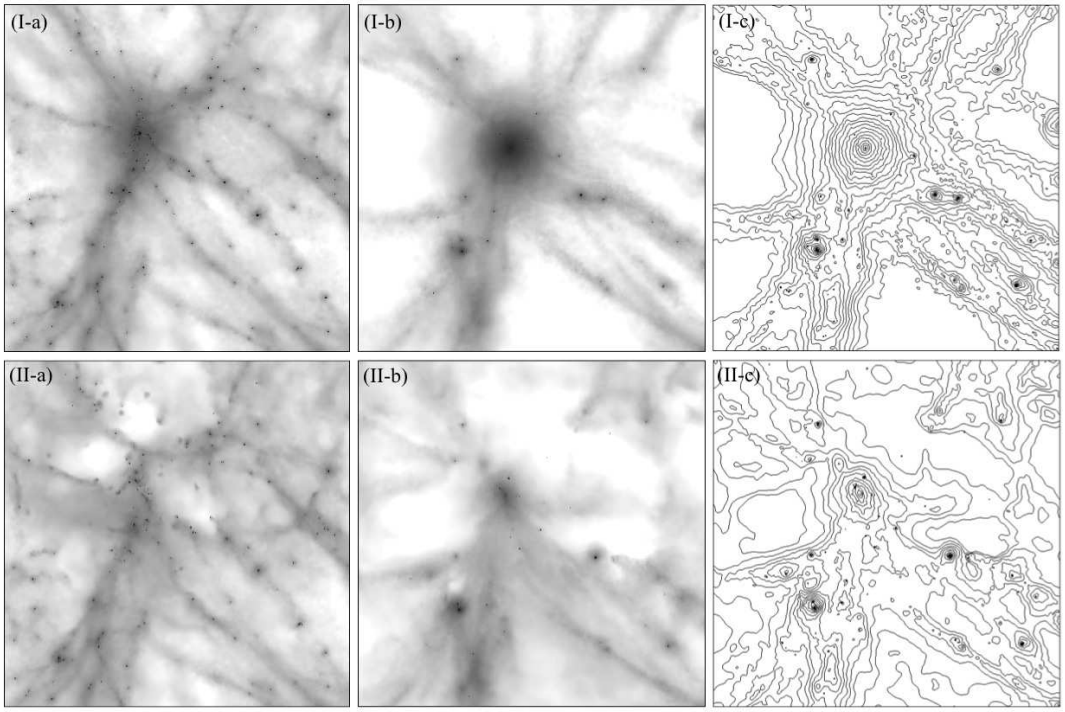

Figure 6. Projected gas density maps for a typical central galaxy with a halo mass of $5 \times 10^{12}\, h^{-1}\, \mathrm{M}_{\odot}$ for the traditional thermal AGN feedback in the top panels, and for the momentum AGN feedback in the bottom panels. The projected gas density maps at $z = 1.5$ are shown in the left-most panels (I-a, II-a), and maps at $z = 0$ are shown in the middle panels (I-b, II-b). Coutours of projected gas density at $z = 0$ are shown in right-most panels (I-c, II-c). The images are 4 Mpc on a side and brighter colour indicates a lower density. While the ThAGN model does not generate any high velocity outflows and bubbles as shown in upper panels, in the MrAGN model the high velocity winds with $v_{\mathrm{w}} \sim 10,000$ km s^{-1} effectively shock the ambient gas and generate cavities around the central massive galaxies in panel (II-a). Bubbles further expand and effectively lower the gas density around the central elliptical galaxy in panels (II-b) and (II-c).

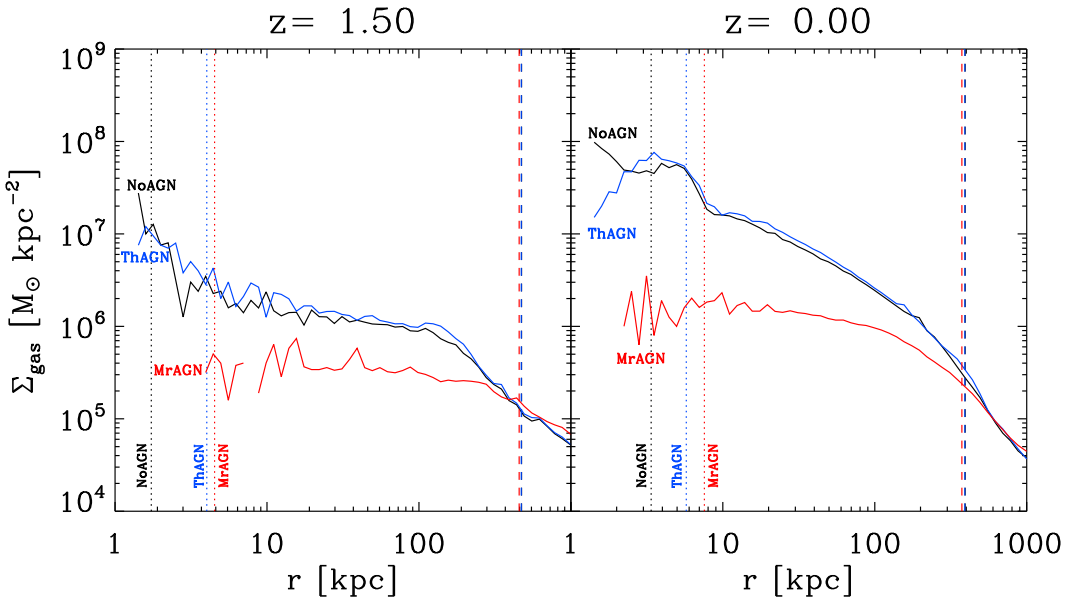

Figure 7. Projected gas density profiles of the central galaxies in a zoom-in simulation of a $5 \times 10^{12}\, h^{-1}\, \mathrm{M}_{\odot}$ dark matter halo at $z = 1.5, 0$ (left and right panel) for the model without AGN feedback (NoAGN, black), thermal feedback (ThAGN, blue), and momentum feedback (MrAGN, red). The virial radius r_{vir} and effective radius r_{eff} of each model are shown in dashed lines and dotted lines respectively. The gas density in the momentum feedback model (MrAGN) is already lower than the others at $z = 1.5$ in all radii within r_{vir}, and the central density becomes ~ 20 times lower at $z = 0$. The thermal feedback model (ThAGN) and the model without AGN feedback (NoAGN) show very similar profiles at z=1.5, but at $z = 0$ ThAGN shows lower density than NoAGN for $r < 2$ kpc.

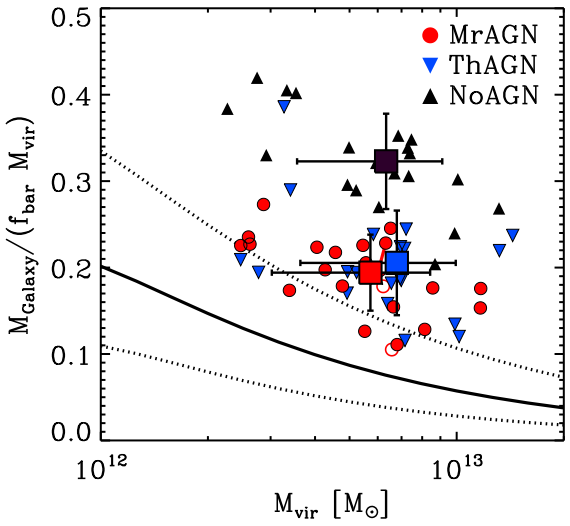

Figure 5. Fraction of baryons that is converted into stars at $z = 0$ for the model without AGN feedback (NoAGN, black triagles), thermal feedback (ThAGN, blue upside down triangles), and momentum and radiative feedback (MrAGN, red circles). The momentum feedback runs without radiative feedback are shown in open red circles for two halos. Respective mean values (and their scatter) are indicated by the squares. The AGN feedback models have lower conversion efficiencies than the NoAGN model but are still a factor of 2 higher than abundance matching estimates from Moster et al. (2013) (solid black line).

fraction thereof that is converted into stars in the simulated central galaxy. For simulated galaxies with NoAGN model, the fraction declines in a roughly linear fashion with the logarithm of the halo mass from $f_* \approx 0.6$ for the smallest halos ($\approx 10^{12} M_\odot$) to $f_* \approx 0.2$ for high mass halos ($\gtrsim 10^{13} M_\odot$), over-predicting by a factor of $\sim 2-3$ than the estimates from recently published work of the conversion efficiencies based on the abundance matching technique (Moster et al. 2013). Note that the conversion efficiencies of NoAGN models we obtain in this study are slightly higher than the value from Oser et al. (2012). Using the modified SPH version which allows for more efficient mixing we find that more gas cools resulting in higher conversion efficiencies. In case of AGN feedback models, both ThAGN and MrAGN models show lower conversion efficiencies compared to NoAGN models, but they still over-predict by a factor of ~ 2 than the estimates and are expected to further increase if metalline cooling was included. This seems to be due to the absence of the ejective supernova wind feedback, which is especially important for low-mass systems. Our simulations do not generate significant winds in the low-mass systems which do not have massive black holes, and thus overestimate the condensed baryon fraction of low-mass galaxies that can accrete onto high mass galaxies at late stages of evolution. This may produce a factor of 2 discrepancy for high-mass galaxies because of over-predicted accreted stars from the low-mass galaxies. The discrepancy is expected to be effectively reduced by including wind stellar feedback, as the work by Ciotti et al. (1991) has shown that Type I SN in normal ellipticals is capable of ejecting significant fraction of the secondary gas from the systems. In recent study by Hirschmann et al. (2013), galactic winds driven by SN are found to be effective in suppressing central star formation in less massive systems.

3.4 Gas mass fraction and Star formation rate

One of the most important findings in the MrAGN feedback models is the effective AGN-driven quenching of star formation in central galaxies in consistent with the observation (e.g. Page et al. 2012). The high velocity outflowing winds shock the ambient gas and generate cavities around the central massive galaxies, significantly lowering the gas density and suppressing star formation in MrAGN model.

To illustrate this effect, in Figure 6 we show the projected gas density maps of the central galaxies at $z = 1.5, 0$ in a zoom-in simulation of a $5 \times 10^{12}\, h^{-1}\, M_\odot$ dark matter halo with the ThAGN feedback, and with the MrAGN feedback. While the ThAGN model does not generate any high velocity outflows and bubbles, in the MrAGN model the high velocity winds with $v_w \sim 10,000$ km s^{-1} effectively shock the ambient gas and generate cavities around the central massive galaxies. Bubbles further expand and effectively lower the gas density around the central elliptical galaxy.

The gas density lowered by the AGN wind is quantitatively shown in Figure 7. It shows the projected gas density profiles of the central galaxies at $z = 1.5, 0$ in a zoom-in simulation of a $5 \times 10^{12}\, h^{-1}\, M_\odot$ dark matter halo, identical galaxies shown in Figure 6. The gas density in the momentum feedback model (MrAGN) is already lower than the others at $z = 1.5$ in all radii within r_{vir}, and the central density becomes ~ 20 times lower at $z = 0$. The thermal feedback model (ThAGN) and the model without AGN feedback (NoAGN) show very similar profiles at z=1.5. At $z = 0$ ThAGN shows lower density than NoAGN but only for $r < 2$ kpc. The ThAGN models have localized effects within $r < 2$ kpc.

In Figure 8 we compare the gas mass fraction of all simulated halos to observation. We measure the fraction of gas mass to the total mass within r_{500}, the radius where the spherical over-density drops below 500 times the critical density of the universe at $z = 0$. The observed $f_{gas,500} - M_{500}$ relation derived from 43 nearby galaxy groups with $M_{500} = 10^{13-14}\, M_\odot$ from Sun et al. (2009) is shown in black solid line with 1σ scatter in dotted lines. We also overplot the observed gas mass fraction of galaxy groups from Sun et al. (2009) in black crosses. In MrAGN model, the strong wind results in much lower gaseous mass fraction compared to other feedback models especially for the low mass galaxies. The differences between MrAGN and other feedback models becomes smaller as MrAGN model show higher gaseous mass fraction in higher mass galaxies. This is consistent with the observed relation which shows a strong trend in gas mass fraction with total mass, such that galaxy groups have significantly lower fractions compared to massive clusters and the universal baryon fraction $f_b = 0.17$. McCarthy et al. (2011); Le Brun et al. (2014) also previously showed that a model with AGN feedback can reproduce X-ray luminosity and gas mass fractions of groups and clusters of galaxies.

In Figure 9 we show the median star formation rate over time with the various feedback models, considering stars within the 10% of the virial radius (r_{10}) of the galaxy centre. In MrAGN model (red), the AGN feedback drives a large-

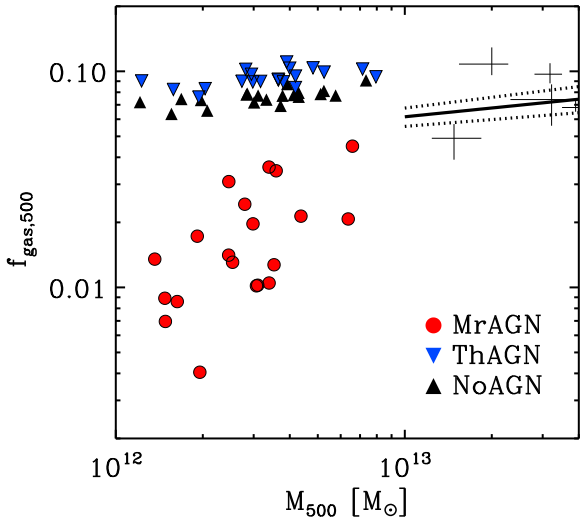

Figure 8. The enclosed gas mass fraction within r_{500}, $f_{\rm gas,500} - M_{500}$ relation for the different AGN feedback models: NoAGN in black triangles, ThAGN in blue upside down triangles and MrAGN in red circles. The black crosses and black solid lines are the observed data and fitted $f_{\rm gas,500} - M_{500}$ relation of the nearby galaxy groups of $M_{500} = 10^{13-14}$ M$_\odot$ from Sun et al. (2009).

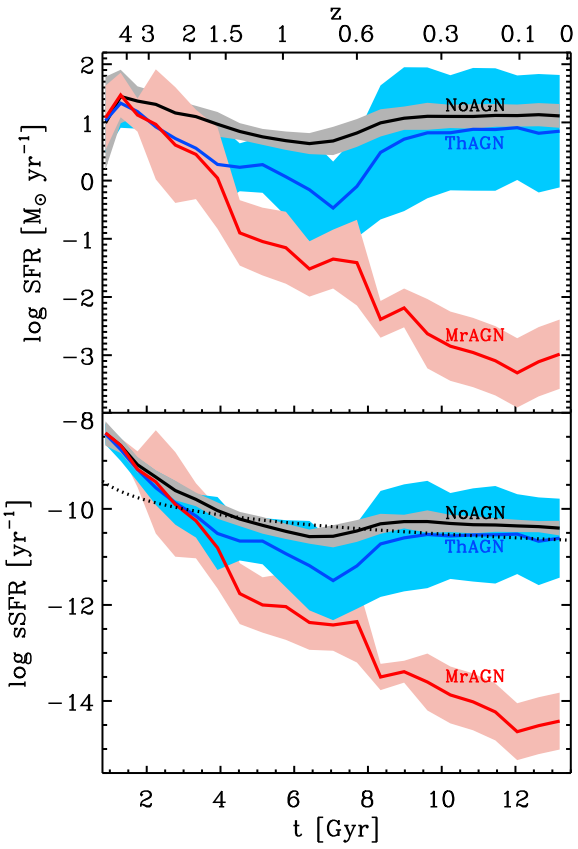

Figure 9. Top: Averaged star formation rate over time for the central galaxies for the model without AGN feedback (NoAGN, black), thermal feedback (ThAGN, blue), and momentum and radiative feedback (MrAGN, red) measured within the 10 % of the virial radii. The median star formation rate for each model are shown in solid lines and the coloured areas show the 1σ scatter of the mean star formation rates. Bottom: same as in the top panel but for the median specific star formation rates. The dotted line indicates the specific star formation rates equal to $0.3/t_{\rm H}$, commonly adopted criteria separating quiescent and star forming galaxies (e.g. Franx et al. 2008). Sources above this line are in a star forming mode: NoAGN feedback model (black) stays above this line through out. Star formation in ThAGN model (blue) is reduced below $0.3/t_{\rm H}$ at $z \sim 1.5$ but increases again as gas cools and falls back again. In the MrAGN feedback model (red), the AGN feedback drives a large-scale wind and effectively quenches star formation.

scale wind that removes nearly all of the residual gas from the galaxy, effectively and rapidly quenching star formation. Compared to the commonly adopted criteria for star forming galaxies, sSFR $> 0.3/t_{\rm H}$, where $t_{\rm H}$ is the age of the universe at each redshift (e.g. Franx et al. 2008, marked with dotted line in the bottom panel), MrAGN model galaxies can be considered quiescent since $z \sim 2$. When AGN feedback is not included, central galaxies keep star-forming and they are classified as star-forming galaxies throughout the simulations. In ThAGN model, in-situ star formation is quenched around $z = 1$, but the star formation rate increases again as cooled gas fall back to the central region. The late time star formation rate is seen to be more than two orders of magnitude lower in the MrAGN than in the ThAGN model. The MrAGN model will be further tested by comparing the star formation activities of the larger sample of simulated galaxies to observations in a forthcoming paper.

3.5 Galaxy sizes and velocity dispersions

In Figure 10, we show the projected half-mass radii of simulated galaxies of MrAGN model as a function of their stellar masses at $z = 0$. We determine the effective radius of the galaxy $r_{\rm eff}$ by determining the mean values of the half-mass radii of all stars within 10% of the virial radius $r_{10} = 0.1 \times r_{\rm vir}$ projected along the three principal axes of the main stellar body. The blue/black/red dashed lines indicate the observed size–mass relation for early-type galaxies respectively from Shen et al. (2003), Hyde & Bernardi (2009), and Nipoti et al. (2009), with the 1σ scatter indicated by the dotted lines. We show the half-mass radius and the stellar mass of the simulated galaxies with a normal density-dependent SPH formulation, consistent with Oser et al. (2012), in open black triangle. The corresponding NoAGN models simulated with the new pressure-entropy formulation are connected with black dotted lines. The SPH-Gal with improved mixing typically reduces the sizes by on average ∼30 percent and also increases the stellar masses compared to normal SPH runs. When AGN feedback is included there is a factor of 2–3 increase in size compared to the NoAGN models.

Figure 11 shows the relation between the velocity dispersion σ of simulated galaxies and their stellar masses (Faber-Jackson relation, Faber & Jackson 1976) for MrAGN model at $z = 0$. We obtain the line-of-sight velocity dispersions σ within $0.5 \times r_{\rm eff}$ along the three principal axes and compare to observations. The observed relations are from Nipoti et al. (2009) who used the SLACS sample of local early-type galaxies at $z = 0$ and Taranu et al. (2013) who

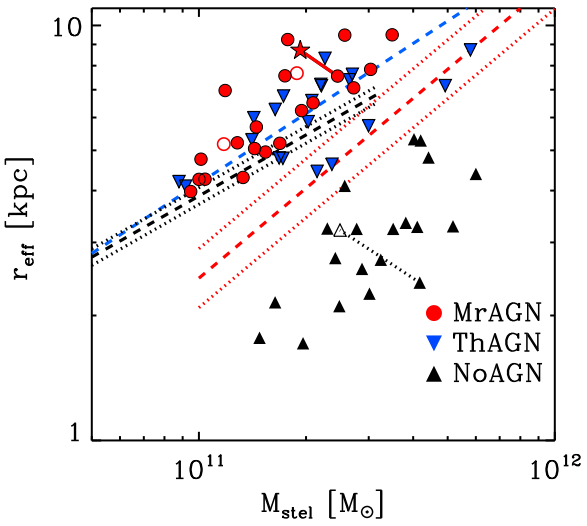

Figure 10. Projected stellar half-mass radii of the simulated galaxies versus stellar masses for redshifts z=0 for the model without AGN feedback (NoAGN, black triangles), thermal feedback (ThAGN, blue upside down triangles), and momentum and radiative feedback (MrAGN, red circles). The blue/black/red dashed lines indicate the observed size–mass relation for early-type galaxies respectively from Shen et al. (2003), Hyde & Bernardi (2009), and Nipoti et al. (2009) with the 1σ scatter indicated by the dotted lines. The momentum feedback runs without radiative feedback are shown in open red circles for two halos. Open black triangle shows the half-mass radius of the simulated galaxy with a density-dependent SPH formulation, consistent with Oser et al. (2012).

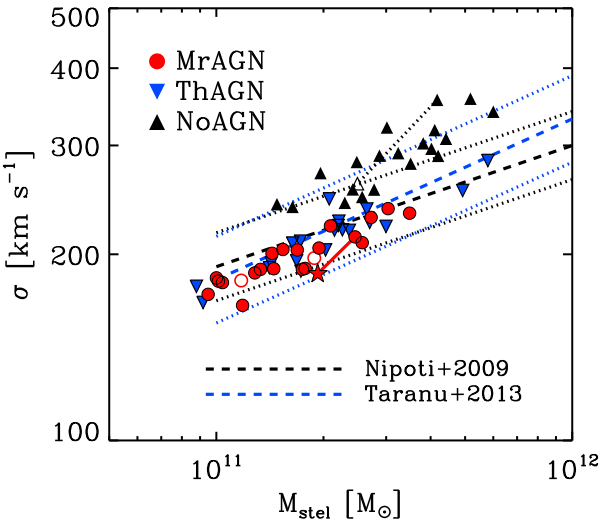

Figure 11. Central (within 0.5 $r_{\rm eff}$) projected velocity dispersion as a function of stellar masses at z=0 for the model without AGN feedback (NoAGN, black triangles), thermal feedback (ThAGN, blue upside down triangles), and momentum and radiative feedback (MrAGN, red circles). The momentum feedback runs without radiative feedback are shown in open red circles for two halos. The black/blue dashed lines indicate the observed relation for early-type galaxies from Nipoti et al. (2009) and Taranu et al. (2013) respectively. We indicate the observed 1σ scatter with the dotted lines. Open black triangle shows the velocity dispersion of the simulated galaxy with a density-dependent SPH formulation, consistent with Oser et al. (2012).

analyzed Nair & Abraham (2010) SDSS catalog. Compared to the observation, ThAGN and MrAGN models predict reasonable velocity dispersions in agreement with Oser et al. (2012).

4 SUMMARY

In this paper, we have run three sets of cosmological hydrodynamic simulations of 20 halos with masses between $2.3 \times 10^{12}\,{\rm M}_\odot \lesssim M_{\rm vir} \lesssim 1.4 \times 10^{13}\,{\rm M}_\odot$ using a modified GADGET-3 SPH code with different AGN feedback models: (1) No black hole and AGN feedback (NoAGN), (2) the standard thermal AGN feedback (ThAGN) (e.g. Di Matteo et al. 2005; Springel et al. 2005; Sijacki et al. 2007; Di Matteo et al. 2008) and (3) mechanical/radiation AGN feedback (MrAGN) (Choi et al. 2012, 2014). We study the effects of AGN feedback on the black-holes and the properties of their host galaxies, i.e. black-hole scaling relation ($M_{\rm BH} - \sigma$ and $M_{\rm BH}/M_{\rm stel}$), X-ray luminosity, stellar and gaseous baryonic conversion efficiencies, star formation, and size of the elliptical galaxies.

We show that massive, non-relativistic outflows and X-ray heating in mechanical and radiation AGN feedback model indeed provide a viable mechanism to regulate the black hole growth in central early type galaxies. The observed $M_{\rm BH} - \sigma$ relationship between the black hole mass and the galaxy velocity dispersion is successfully recovered with the MrAGN model. This was also obtained in the previous ThAGN feedback treatments (e.g. Di Matteo et al. 2005; Springel et al. 2005), and we confirm their results on the observed physical relation between black hole and galactic properties, with our modified SPH code and cosmological simulations. Most importantly, however, the MrAGN model shows much lower X-ray luminosity compared to the commonly adopted ThAGN model where all the feedback energy is distributed locally as thermal heating. While the thermal feedback model produces ∼2-3 orders of magnitude higher thermal X-ray luminosity than expected for given stellar mass of the galaxy, the MrAGN model can successfully reproduce both the observed $L_X - \sigma$ and $M_{\rm BH} - \sigma$ relations.

We show that mechanical and radiation feedback can also effectively suppress in-situ star formation in high mass galaxies as the gas is effectively expelled by AGN-driven outflows especially at late times. The MrAGN model produces massive red and dead galaxies, reducing final stellar mass by a factor of two compared to the previous works without AGN feedback (Oser et al. 2010, 2012) and reducing the final star formation rates by over 10^3 compared with the no AGN feedback or thermal AGN feedback models. Our simulated galaxies with AGN feedback show lower baryonic conversion efficiencies than the ones without AGN feedback, but our samples are still overly efficient in transforming gas into stars. The baryonic conversion efficiencies at $z = 0$ in our simulated galaxies with the MrAGN feedback are still overestimated by roughly a factor of ~ 2 compared to recent predictions (Moster et al. 2013) and would be even en-

hanced if metal-line cooling was included. As AGN feedback mainly affects massive galaxies with massive black holes and quenches star formation in the inner region, 'in-situ' star formation is significantly suppressed in our models resulting lower fraction of in-situ stars compared to the previous models without AGN feedback. One or more missing further mechanisms is needed to reduced the star formation in low mass satellite galaxies that are eventually accreted., e.g. supernova wind feedback (Murray et al. 2005; Oppenheimer & Davé 2006; Hirschmann et al. 2012, 2013; Puchwein & Springel 2013), cosmic ray driven winds (Booth et al. 2013; Hanasz et al. 2013; Salem & Bryan 2014), and/or star formation driven wind (Agertz & Kravtsov 2014; Hopkins et al. 2014). The late time quenching can be more challenging for both ThAGN and MrAGN models as the material removed from lower mass progenitors can be accreted to more massive ones at later times (Oppenheimer et al. 2010).

ACKNOWLEDGMENTS

We benefited from useful conversations with Renyue Cen, Taysun Kimm, Rachel Somerville, James M. Stone, and Michael A. Strauss. We also thank the anonymous referee for many constructive suggestions, which helped to improve the presentation of the results. E.C. and J.P.O. acknowledge the support of NSF grant AST-0707505. E.C. and T.N. acknowledge the support from the DFG cluster of excellence "Origin and Structure of the Universe". E.C. was supported by the Samsung Scholarship foundation and made extensive use of the computing facilities of the Princeton Institute of Computational Science and Engineering.

REFERENCES

Agertz O., Kravtsov A. V., 2014, ArXiv e-prints, 1404.2613
Agertz O. et al., 2007, MNRAS, 380, 963
Behroozi P. S., Conroy C., Wechsler R. H., 2010, ApJ, 717, 379
Bondi H., 1952, MNRAS, 112, 195
Bondi H., Hoyle F., 1944, MNRAS, 104, 273
Booth C. M., Agertz O., Kravtsov A. V., Gnedin N. Y., 2013, ApJ, 777, L16
Booth C. M., Schaye J., 2009, MNRAS, 398, 53
Booth C. M., Schaye J., 2011, MNRAS, 413, 1158
Boroson B., Kim D.-W., Fabbiano G., 2011, ApJ, 729, 12
Bower R. G., Benson A. J., Malbon R., Helly J. C., Frenk C. S., Baugh C. M., Cole S., Lacey C. G., 2006, MNRAS, 370, 645
Burkert A., Tremaine S., 2010, ApJ, 720, 516
Choi E., Naab T., Ostriker J. P., Johansson P. H., Moster B. P., 2014, MNRAS, 442, 440
Choi E., Ostriker J. P., Naab T., Johansson P. H., 2012, ApJ, 754, 125
Ciotti L., D'Ercole A., Pellegrini S., Renzini A., 1991, ApJ, 376, 380
Ciotti L., Ostriker J. P., Proga D., 2010, ApJ, 717, 708
Cox T. J., Di Matteo T., Hernquist L., Hopkins P. F., Robertson B., Springel V., 2006, ApJ, 643, 692
Crenshaw D. M., Kraemer S. B., George I. M., 2003, ARA&A, 41, 117
Croton D. J. et al., 2006, MNRAS, 365, 11
Cullen L., Dehnen W., 2010, MNRAS, 408, 669
De Lucia G., Blaizot J., 2007, MNRAS, 375, 2
Debuhr J., Quataert E., Ma C.-P., 2011, MNRAS, 412, 1341
Debuhr J., Quataert E., Ma C.-P., 2012, MNRAS, 420, 2221
Debuhr J., Quataert E., Ma C.-P., Hopkins P., 2010, MNRAS, 406, L55
DeGraf C., Di Matteo T., Khandai N., Croft R., Lopez J., Springel V., 2012, MNRAS, 424, 1892
Dehnen W., 2001, MNRAS, 324, 273
Dehnen W., Aly H., 2012, MNRAS, 425, 1068
Di Matteo T., Colberg J., Springel V., Hernquist L., Sijacki D., 2008, ApJ, 676, 33
Di Matteo T., Khandai N., DeGraf C., Feng Y., Croft R. A. C., Lopez J., Springel V., 2012, ApJ, 745, L29
Di Matteo T., Springel V., Hernquist L., 2005, Nature, 433, 604
Dunn J. P. et al., 2010, ApJ, 709, 611
Durier F., Dalla Vecchia C., 2012, MNRAS, 419, 465
Faber S. M., Jackson R. E., 1976, ApJ, 204, 668
Fabian A. C., 2012, ARA&A, 50, 455
Ferrarese L., Merritt D., 2000, ApJ, 539, L9
Forman W., Jones C., Tucker W., 1985, ApJ, 293, 102
Franx M., van Dokkum P. G., Schreiber N. M. F., Wuyts S., Labbé I., Toft S., 2008, ApJ, 688, 770
Gebhardt K. et al., 2000, ApJ, 539, L13
Guo Q. et al., 2011, MNRAS, 413, 101
Guo Q., White S., Li C., Boylan-Kolchin M., 2010, MNRAS, 404, 1111
Haardt F., Madau P., 1996, ApJ, 461, 20
Hanasz M., Lesch H., Naab T., Gawryszczak A., Kowalik K., Wóltański D., 2013, ApJ, 777, L38
Hirschmann M. et al., 2013, MNRAS, 436, 2929
Hirschmann M., Somerville R. S., Naab T., Burkert A., 2012, MNRAS, 426, 237
Hopkins P. F., 2013, MNRAS, 428, 2840
Hopkins P. F., Hernquist L., Cox T. J., Robertson B., Di Matteo T., Springel V., 2006, ApJ, 639, 700
Hopkins P. F., Kereš D., Oñorbe J., Faucher-Giguère C.-A., Quataert E., Murray N., Bullock J. S., 2014, MNRAS, 445, 581
Hoyle F., Lyttleton R. A., 1939, Proceedings of the Cambridge Philosophical Society, 34, 405
Hu C.-Y., Naab T., Walch S., Moster B. P., Oser L., 2014, MNRAS, 443, 1173
Humphrey P. J., Buote D. A., Gastaldello F., Zappacosta L., Bullock J. S., Brighenti F., Mathews W. G., 2006, ApJ, 646, 899
Hyde J. B., Bernardi M., 2009, MNRAS, 394, 1978
Johansson P. H., Naab T., Ostriker J. P., 2009, ApJ, 697, L38
Katz N., White S. D. M., 1993, ApJ, 412, 455
Kauffmann G. et al., 2003, MNRAS, 341, 33
Khandai N., Feng Y., DeGraf C., Di Matteo T., Croft R. A. C., 2012, MNRAS, 423, 2397
Kim D.-W., Fabbiano G., 2013, ApJ, 776, 116
Kormendy J., Ho L. C., 2013, ARA&A, 51, 511
Kormendy J., Richstone D., 1995, ARA&A, 33, 581
Le Brun A. M. C., McCarthy I. G., Schaye J., Ponman T. J., 2014, MNRAS, 441, 1270

Magorrian J. et al., 1998, AJ, 115, 2285
Marconi A., Hunt L. K., 2003, ApJ, 589, L21
Martizzi D., Teyssier R., Moore B., Wentz T., 2012, MNRAS, 422, 3081
Mathews W. G., Brighenti F., 2003, ARA&A, 41, 191
Mathews W. G., Brighenti F., Faltenbacher A., Buote D. A., Humphrey P. J., Gastaldello F., Zappacosta L., 2006, ApJ, 652, L17
McCarthy I. G., Schaye J., Bower R. G., Ponman T. J., Booth C. M., Dalla Vecchia C., Springel V., 2011, MNRAS, 412, 1965
McCarthy I. G. et al., 2010, MNRAS, 406, 822
McConnell N. J., Ma C.-P., 2013, ApJ, 764, 184
McKee C. F., Ostriker J. P., 1977, ApJ, 218, 148
Moe M., Arav N., Bautista M. A., Korista K. T., 2009, ApJ, 706, 525
Moster B. P., Naab T., White S. D. M., 2013, MNRAS, 428, 3121
Moster B. P., Somerville R. S., Maulbetsch C., van den Bosch F. C., Macciò A. V., Naab T., Oser L., 2010, ApJ, 710, 903
Murray N., Quataert E., Thompson T. A., 2005, ApJ, 618, 569
Naab T., Johansson P. H., Ostriker J. P., 2009, ApJ, 699, L178
Naab T., Johansson P. H., Ostriker J. P., Efstathiou G., 2007, ApJ, 658, 710
Nair P. B., Abraham R. G., 2010, ApJS, 186, 427
Nipoti C., Treu T., Auger M. W., Bolton A. S., 2009, ApJ, 706, L86
Novak G. S., Ostriker J. P., Ciotti L., 2011, ApJ, 737, 26
Oppenheimer B. D., Davé R., 2006, MNRAS, 373, 1265
Oppenheimer B. D., Davé R., Kereš D., Fardal M., Katz N., Kollmeier J. A., Weinberg D. H., 2010, MNRAS, 406, 2325
Oser L., Naab T., Ostriker J. P., Johansson P. H., 2012, ApJ, 744, 63
Oser L., Ostriker J. P., Naab T., Johansson P. H., Burkert A., 2010, ApJ, 725, 2312
Ostriker J. P., Choi E., Ciotti L., Novak G. S., Proga D., 2010, ApJ, 722, 642
Page M. J. et al., 2012, Nature, 485, 213
Planck Collaboration et al., 2013, ArXiv e-prints, 1303.5062
Proga D., Kallman T. R., 2004, ApJ, 616, 688
Proga D., Stone J. M., Kallman T. R., 2000, ApJ, 543, 686
Puchwein E., Springel V., 2013, MNRAS, 428, 2966
Read J. I., Hayfield T., 2012, MNRAS, 422, 3037
Rigby E. E., Best P. N., Brookes M. H., Peacock J. A., Dunlop J. S., Röttgering H. J. A., Wall J. V., Ker L., 2011, MNRAS, 416, 1900
Ritchie B. W., Thomas P. A., 2001, MNRAS, 323, 743
Saitoh T. R., Makino J., 2009, ApJ, 697, L99
Saitoh T. R., Makino J., 2013, ApJ, 768, 44
Salem M., Bryan G. L., 2014, MNRAS, 437, 3312
Sazonov S. Y., Ostriker J. P., Ciotti L., Sunyaev R. A., 2005, MNRAS, 358, 168
Shen S., Mo H. J., White S. D. M., Blanton M. R., Kauffmann G., Voges W., Brinkmann J., Csabai I., 2003, MNRAS, 343, 978
Sijacki D., Springel V., Di Matteo T., Hernquist L., 2007, MNRAS, 380, 877
Sijacki D., Springel V., Haehnelt M. G., 2009, MNRAS, 400, 100
Silk J., Rees M. J., 1998, A&A, 331, L1
Simpson C. M., Bryan G. L., Hummels C., Ostriker J. P., 2014, ArXiv e-prints, 1410.3822
Somerville R. S., Hopkins P. F., Cox T. J., Robertson B. E., Hernquist L., 2008, MNRAS, 391, 481
Spergel D. N. et al., 2007, ApJS, 170, 377
Spergel D. N. et al., 2003, ApJS, 148, 175
Springel V., 2005, MNRAS, 364, 1105
Springel V., Di Matteo T., Hernquist L., 2005, MNRAS, 361, 776
Springel V., Hernquist L., 2003, MNRAS, 339, 289
Sun M., Voit G. M., Donahue M., Jones C., Forman W., Vikhlinin A., 2009, ApJ, 693, 1142
Taranu D. S., Dubinski J., Yee H. K. C., 2013, ApJ, 778, 61
Teyssier R., Moore B., Martizzi D., Dubois Y., Mayer L., 2011, MNRAS, 414, 195
Tremaine S. et al., 2002, ApJ, 574, 740
Trinchieri G., Fabbiano G., 1985, ApJ, 296, 447
Ueda Y., Akiyama M., Ohta K., Miyaji T., 2003, ApJ, 598, 886
Vogelsberger M., Genel S., Sijacki D., Torrey P., Springel V., Hernquist L., 2013, MNRAS, 436, 3031